ABSORBING CROSS SECTION IN REVERBERATION CHAMBER: EXPERIMENTAL AND NUMERICAL RESULTS

G. Gradoni[1], D. Micheli[2], F. Moglie[3, *], and V. Mariani Primiani[3]

[1]Institute for Research in Electronics and Applied Physics, University of Maryland, College Park, MD 20742, USA

[2]Sapienza Università di Roma, Dipartimento di Ingegneria Astronautica Elettrica ed Energetica, Area Ingegneria Astronautica, Via Salaria 851, Roma 00138, Italy

[3]DII — Università Politecnica delle Marche, Via Brecce Bianche 12, Ancona 60131, Italy

Abstract—Reverberation chamber (RC) test facility allows to determine the absorbing cross section (ACS) of lossy materials under a random field excitation. Measurements are based on the quality factor variation produced by the sample under test presence with respect to the empty chamber condition. Simulations are based on the representation of the RC electromagnetic field by means of a random plane wave superposition. A finite-difference time-domain code is used to compute the material absorbed power and to recover a numerical ACS. The method sensibility is stressed by application to small size samples. Comparison between numerical and experimental data reveals a satisfactory agreement. Results for different materials are presented in the paper: soft foam absorbers, carbon foam sheets, and carbon/carbon sheets.

1. INTRODUCTION

In microwave engineering, applied to communications, military, or industrial contexts, a precise knowledge on electromagnetic properties of materials is often required. Measurement methods are typically based on the acquisition of the transmission and the reflection

coefficients measured inserting a material sample inside a coaxial or a waveguide fixture. Non resonant transmission/reflection methods are very simple and give acceptable accuracy over a broadband frequency range [1, 2]. These methods have been refined along the years to overcome some problem arising in the case of small losses and multiple solutions in broadband measurements [3]. Materials are often used to produce absorbing foam sheets or objects with complex geometry (pyramidal absorbers for example), to be used to minimize the radar cross section (RCS) of targets or to assemble anechoic chambers. In this cases, reflection measurements are carried out on large samples, or directly on-site measurement are done [4–8]. Although, permittivity and permeability are intrinsic properties of the materials, absorption properties of large panels or walls depend also on geometry, incoming wave polarization and direction of incidence. Therefore, the complete characterization of their absorption properties requires the repetition of the measurement using several angles of incidence and polarizations. In real world the excitation of such structures exhibits random characteristics, and therefore the evaluation of absorption for a particular condition could be meaningless. To overcome this limitation, the reverberation chamber (RC) represents an excellent way to excite the absorbing material in a completely random way. In fact, RCs are large overmoded cavities wherein the electromagnetic field is statistically uniform and isotropic and without a prefixed polarization [9, 10]. The above mentioned field properties are achieved by the presence of rotating paddles, that strongly changes field boundary conditions due to their electrically large dimensions [11–13].

Moreover, RC field characteristics are able to create real environment propagation conditions, very useful in Wi-Fi communication system testing [14–17], and in the antenna testing [18]. On the other hand, also the studies of human exposure to electromagnetic field take benefit from RC in order to reproduce real exposure conditions [19, 20]. RCs are successfully used to characterize materials and structures from a shielding point of view, also considering composite materials for architectural shielding [21–23]. Moreover, it was demonstrated that the complex random field created inside an RC can be numerically simulated using a finite summation of random plane waves [24, 25], which makes straightforward to predict the behavior of complex equipment placed inside an RC [26–29]. In this context, the present paper considers the penetration of the RC field inside a lossy material in order to characterize its absorbing properties. The problem is faced both numerically and experimentally. The numerical approach is based on the computation of the power absorbed by the sample under test through the plane wave representation of the chamber field. The interaction be-

tween each plane wave of the summation and the sample under test is treated by the finite-difference time-domain (FDTD) method using an ad-hoc numerical code. The knowledge of the absorbed power allows to retrieve the absorption cross section (ACS) of the material [30, 31] and RCS [32]. From a practical point of view, the ACS is recovered measuring the quality factor (Q factor) variation between the empty chamber condition and the loaded chamber condition, when the sample is inserted in. It must be remarked that the power of the simulation tool consists in the possibility to account for whatever type of absorber geometry, allowing the prediction of the absorbing capability during the early design stage when the right compromise between material permittivity (and/or permeability) and absorber geometry is sought.

2. RC MEASUREMENT SETUP

The adopted RC dimension is $6.00\,\mathrm{m} \times 4.00\,\mathrm{m} \times 2.50\,\mathrm{m}$ so that its fundamental mode resonance frequency is $f_0 = 45.04\,\mathrm{MHz}$, giving a lower usable frequency (LUF) of about $6f_0 = 270\,\mathrm{MHz}$. Both horizontal and vertical stirrers equip the chamber. The vertical stirrer is a Z-folded paddle with height $2.4\,\mathrm{m}$ and width $1.2\,\mathrm{m}$. The horizontal stirrer consists of four metallic panels connected by aluminum foils to give it a rotation volume similar to that of the other stirrer, Figure 1. Both stirrers are moved in a stepped mode by independent engines, which assure a $1°$ degree resolution. Transmitting and receiving antennas are two double ridge (EMCO 3115 and AH Systems SAS-571). To avoid any possible direct illumination, responsible for statistics degradation in the received power, they are cross polarized and oriented toward the chamber opposite corners. A VNA (Agilent
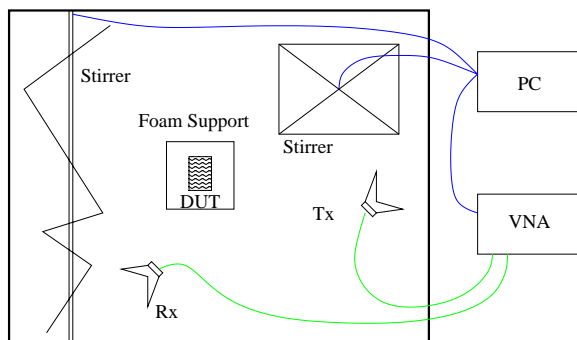
Figure 1. Chamber, stirrers, and material under test. The dimensions of the chamber are $4.00 \times 6.00 \times 2.50\,\mathrm{m}^3$.

Figure 2. Inner view of the chamber. Foreground on the left, it is visible a part of a stirrer, then the sample under test on a support of foamed polystyrene. The other stirrer is visible on the center and the two double ridge antennas are on the right.

Technologies model E5071B) is used to measure the transmission coefficient between the two antennas, after an adequate calibration able to compensate for the antenna cable attenuation. In the present work, measurements were carried out in the range 2–8 GHz, subdivided into 3 sub-ranges, and using 1601 frequency points in each sub-range. A 500 Hz IF bandwidth was set for the VNA to reduce noise and a 5 seconds sweep time was set for each range. In this way, a sufficient frequency resolution (1.25 MHz) was reached to allow a good frequency stirring. Moreover, measurements were repeated in 36 stirrer independent positions to add also a mechanical stirring process for a better Q factor evaluation. The 36 positions were obtained interleaving 6 positions for each stirrer [11]. Figure 2 shows a photograph of the chamber inner view. The absorbing material sample was placed over a polystyrene foam support and oriented avoiding any alignments along the chamber Cartesian axes.

3. ACS DETERMINATION IN RC

Inside an RC a single instant measurement is meaningless and all electromagnetic quantities have to be ensemble averaged over the stirrer rotation. Therefore, the average ACS is defined as

$$ACS = \frac{\langle P_s \rangle}{S_i}, \tag{1}$$

where P_s is the power dissipated by the sample and $S_i = \langle |E_T|^2 \rangle / \eta_0$ the incident scalar power density. The symbol $\langle \cdot \rangle$ means an ensemble average over the stirrer rotation and frequency stirring, and η_0 is the free space wave impedance. In such a definition, it is assumed the statistical uniformity of the total field magnitude $|E_T|$, with asymptotic distribution χ_6 (chi-distribution with 6 degrees of freedom) [9].

Spectral characteristics of a mode-stirred cavity are sensible to energy perturbations (such as a low-loss dielectric inclusion), because of the strong modal overlapping featuring the overmoded regime. The total losses inside an RC is due to many mechanisms: wall losses, antenna losses, and material sample losses. Say Q_u the Q factor measured without the material sample and Q_l that measured with the sample inside the chamber, the contribution Q_s due to the sample dissipation only is

$$Q_s^{-1} = Q_l^{-1} - Q_u^{-1}. \tag{2}$$

In terms of stored energy and dissipated power

$$Q_s = \frac{\omega W}{\langle P_s \rangle} = \frac{\omega S_i V}{c \langle P_s \rangle}, \tag{3}$$

where ω is the angular frequency of excitation, W the energy stored by the chamber, V the chamber volume, and c speed of light in vacuum. On substituting (1) into (3) and unfolding, yields

$$ACS = \frac{\omega V}{c Q_s} = \frac{2\pi V}{\lambda Q_s}, \tag{4}$$

where λ is the wavelength at operation frequency of the chamber. Indirect estimation of ACS passes through insertion loss measurements [33] (with and without the material sample) by the well-known definition

$$Q = \frac{16\pi^2 V \langle P_r \rangle}{\lambda^3 \eta_{Tx} \eta_{Rx} \langle P_t \rangle} = \frac{16\pi^2 V \left\langle |S_{21}|^2 \right\rangle}{\lambda^3 \eta_{Tx} \eta_{Rx}}, \tag{5}$$

where P_r is the power captured by the receiving antenna Rx with total efficiency η_{Rx}, P_t the power injected by the transmitting antenna Tx with total efficiency η_{Tx}, and S_{21} the transmission scattering parameter between port 1, connected to Tx, and port 2, connected to Rx, of a vector network analyzer (VNA). Comparison with simulations follows by direct numerical calculations of (1).

4. FDTD SIMULATION OF THE SAMPLE ACS

In the FDTD code, perpendicular planes to the three Cartesian axes are introduced, each of which are called "separation plane". They
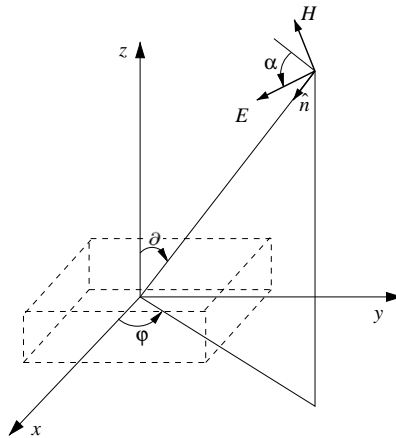
Figure 3. Geometry of a random plane wave incident on the computation volume.

separate the incident fields and the scattered fields. When there is no object in the working volume the fields are located inside the total field region. On one of the separation planes the electric and magnetic fields are calculated adding each component to or subtracting it from the incident fields according to a standard procedure [34]. The incident fields are computed with the analytical method, based on Hill's plane wave model for an RC [9]. The chamber features are sampled by the two parameters N and M. More precisely, M simulations are performed and each simulation uses the superposition of N random plane waves in order to simulate M different positions of the stirring mechanism inside an RC. The parameters of each plane wave are generated in the FDTD initialization phase. They are stored and recalled for each FDTD temporal iteration. Referring to Figure 3, the generated parameters are: angles φ and ϑ, polarization α and the phase of the incident wave. The angles φ and ϑ are generated to have a uniform distribution on a spherical surface. In fact, the incidence $\hat{\mathbf{n}}$ can come from any direction with the same probability [24]. To do this, a spherical surface surrounding the field observation point located at the center of the reference system can be introduced. N points of the sphere can be associated to N directions of arrival of the plane waves of the set, and in order to represent the RC field, they must be uniformly distributed on the surface itself. A simple uniform distribution for angles ϑ and φ would result into a strong gathering of the propagation directions on the poles. To reach the goal, a uniform distribution can

be chosen for φ so that its probability density function (PDF) becomes

$$PDF(\varphi) = \begin{cases} 0 & \text{for } \varphi < 0 \\ 1/(2\pi) & \text{for } 0 \leq \varphi \leq 2\pi \\ 0 & \text{for } \varphi > 2\pi \end{cases}. \tag{6}$$

whereas for ϑ the probability density decreases towards the poles

$$PDF(\vartheta) = \begin{cases} 0 & \text{for } \vartheta < 0 \\ 0.5\sin(\vartheta) & \text{for } 0 \leq \vartheta \leq \pi \\ 0 & \text{for } \vartheta > \pi \end{cases}. \tag{7}$$

Equations (6) and (7) guaranty that the propagation directions are uniformly distributed over the solid angles. The assumption of a uniform distribution for the polarization angle α in the range $[0, 2\pi]$ leads to the absence of a preferred polarization, as in an actual RC. The phase of each single wave, was chosen to have a uniform distribution between 0 and 2π. A detailed description of the procedure used to generate the previous parameters can be found in [35], whereas a broader discussion of this issue can be found in [36].

Finally, a constant value E_0 for each plane wave amplitude is adopted. This choice is allowed if the statistics (calculated over the M different sets of N plane waves) of the total field correspond to those achieved in an ideal chamber. The modulus of the total electric field in an RC exhibits a χ_6 distribution [9]. From this condition, the averaged (over the stirrer rotation) total field amplitude can be derived

$$\langle |E_T| \rangle = \frac{15}{16}\sqrt{\frac{\pi}{3}}\sqrt{N}\,|E_0|, \tag{8}$$

where $\langle |E_T| \rangle$ states for the averaged (over the M sets) value of the total field modulus. This relationship between the averaged total field and the amplitude E_0 of each plane wave is very useful to correlate simulations and measurements. If $\langle |E_T| \rangle$ is measured in the RC, to simulate the field inside this chamber by M sets of N plane waves it is sufficient to assign them the constant amplitude $|E_0|$ according to (8).

The result of each M FDTD simulations is the vector sum in each cell (i, j, k) of the field produced by the N plane waves of the m-th set

$$E_{i,j,k}^{N,m} = \sum_{n=1}^{N} E_{i,j,k}^{n,m}. \tag{9}$$

The knowledge of the $E_{i,j,k}^{N,m}$ field of the sample allows us to compute the dissipated power density in each cell

$$P_{i,j,k}^{N,m} = \frac{\sigma_{i,j,k}\left|E_{i,j,k}^{N,m}\right|^2}{2}, \tag{10}$$

where $\sigma_{i,j,k}$ is the cell conductivity. The total power absorbed by the sample is therefore achieved by summing the dissipated power density in each cell multiplied by its volume $V_{i,j,k}$. Performing the average over the M simulations, we obtain the total averaged power to be inserted in (1) for the ACS computation

$$\langle P_s \rangle = \sum_{m=1}^{M} \sum_{i,j,k} P_{i,j,k}^{N,m} V_{i,j,k}. \tag{11}$$

5. RESULTS

The ACS values were found for three different materials. First of all, we tested some soft foam sheet and pyramidal absorbers, typically used to dump reflection in anechoic chamber walls. For some of these material the conductivity values are known, so we are also able to compare measurements and simulations. Subsequently, some carbon foams samples were measured. These materials exhibit an excellent thermal insulation capability that combined with absorbing proprieties makes them eligible to reduce the vehicle reflection in aerospace applications. Finally, carbon/carbon composite sheets were measured. They are appealing materials for aerospace application because they are lighter than metals, they exhibit high mechanical strength and high electrical conductivity. A sample of all tested materials are shown in the picture of Figure 4.
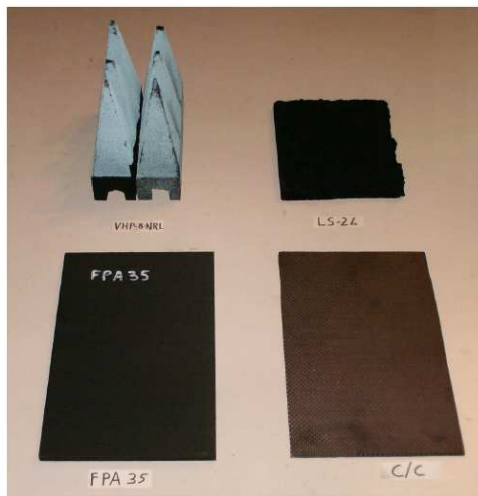

Figure 4. Picture of four samples: VHP-8-NRL pyramids, LS-24 foam sheet, GRAFOAM FPA-35 sheet, and carbon/carbon sheet.

5.1. Soft Material Absorbers

We considered the Eccosorb LS-24 foam sheet (thickness $t = 18\,\text{mm}$) and the VHP-8-NRL pyramidal absorber both from Emerson & Cuming. Figure 5 reports the measured chamber Q factor for the empty chamber, for a $0.6\,\text{m} \times 0.6\,\text{m}$ VHP-8-NRL, for a $0.6\,\text{m} \times 0.38\,\text{m}$ LS-24 and for a small piece of the same LS-24 ($0.20\,\text{m} \times 0.18\,\text{m}$). It can be noted the capability of the chamber to reveal also the presence of a very small, compared to the chamber volume, piece of absorbing material. The accuracy in computing the Q factor is enhanced applying both frequency stirring, over 80 frequency points, and mechanical stirring, over 36 stirrer positions, to perform the ensemble average required in (5). Moreover in applying (5) we assumed $\eta_{Tx} = \eta_{Rx} = 0.9$, as suggested by the IEC standard for similar antennas [37]. After a check of the reflection coefficient, the antennas were considered perfectly matched inside the chamber. In Figure 6, the ACS recovered
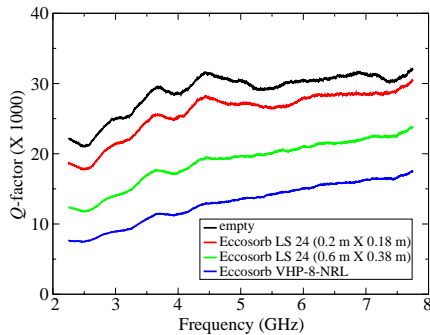
Figure 5. Q factors for the un-loaded RC and for some samples.
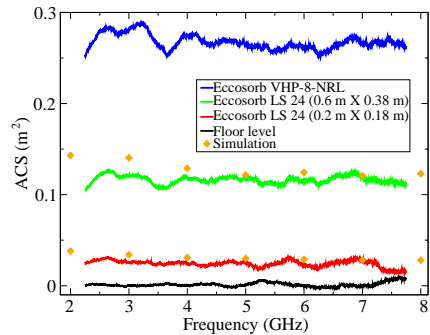
Figure 6. Experimental and computed ACS.

Table 1. LS-24 real and imaginary relative permittivity.

Frequency (GHz)	$\Re\left(\varepsilon_r\right)$	$\Im\left(\varepsilon_r\right)$
2	10	11.5
3	7.5	8
4	6	7.5
5	5.25	7
6	5	6
7	5	5.75
8	4.75	5.5

from Q values according to the procedure of Section 3 is reported for each material. The measurement repeatability was checked changing the material position moving it in the working volume of the RC: the results overlapped. Concerning simulations, we focused the attention on the simulation of both LS-24 pieces, in particular the smallest one allows us to stress the capability of the numerical method, due to the very small dimensions. Table 1 shows the values of the complex permittivity given by manufacturer, and used in the simulations. The computation volume was divided into $280 \times 260 \times 98$ cubic cells whose side is 1 mm, including the material under test, separation planes between total field and scattered field regions, and absorbing boundary conditions. Time step was 1.75 ps. The average quantities are obtained performing $M = 200$ simulations, each one using $N = 100$ random plane waves as excitation. This choice was done after several tests [24]. The number N of plane waves for the superposition, and the number M of simulations are selected as a compromise between the computation time and the statistic convergence of the law of large numbers. In the same Figure 6 the numerical ACS is reported (diamonds) computed adopting the procedure described in Section 4 which recovers the ACS from the computed absorbed power. The sample absorbed power was obtained assuming the complex permittivity values given by the manufacturer for the LS-24 sample. Numerical and experimental results agree well. This means that our simulation technique can be used to design whatever absorber, considering not only material properties but also the shape thanks to the FDTD ability to describe complex geometries. In this case the computer burden can greatly increase. The "embarrassingly parallel" algorithm that solve M independent simulations allowed us to use a cluster of computers, requiring only few hours of computation [12]. Moreover, the FDTD algorithm can be further parallelized due to its simple structure [38].

In Figure 6 it is also reported the floor level corresponding to the minimum measurable ACS. It is obtained repeating the Q factor measurement without inserting anything in the chamber but simply opening and closing the door. Essentially, it reveals the residual uncertainty in measuring the chamber Q factor. This uncertainty mainly depends on the number of independent samples used to estimate the Q factor itself.

5.2. Absorbing Cross Section of Carbon Foams

Three kind carbon foam sheets supplied by GRAFOAM are tested: FPA-5, FPA-10, and FPA-35. They differ from density and cell size. In fact, carbon foams are cellular structures with low mass density. Their mechanical, thermal and electrical properties are strictly dependent on

cell size, shape and 3-D arrangement. These cell parameters determine
the specific bulk material properties, the relative density and porosity
of the foam. Scanning electron microscopy analysis is required to
investigate the morphology of the carbon foam cellular structure [39].
Also the effective conductivity of the foam, and consequently the ACS,
depend on this particular internal morphology. In the present case the
higher is the FPA number, the higher is the material density.

Figure 7 reports the measured ACS for the above three sheet
samples, which dimension is $300 \times 200\,\text{mm}^2$ and thickness $t = 5\,\text{mm}$.
The samples were placed on a expanded polystyrene support. We
can note that carbon foam ACS values are lower than those of soft
absorbing materials, probaly due to the regular cellular structure that
reduce the material density, effective conductivity, so enhancing the
reflection. In fact, less dense materials (FPA-5) exhibits lower ACS.
The effect of the sample thickness was also investigated. Figure 8
reports this analysis for the FPA-5, while Figure 9 reports this analysis
for the FPA-35.

For the tested materials, we can note that the higher is the
material density, the lower is the absorbing capability (lower ACS).
When the density increases, the effective conductivity becomes higher,
enhancing the reflections instead of absorption. On the other hand,
the investigate thickness spread seems to not appreciably influence the
ACS, due to the small variation of exposed surface and to the low
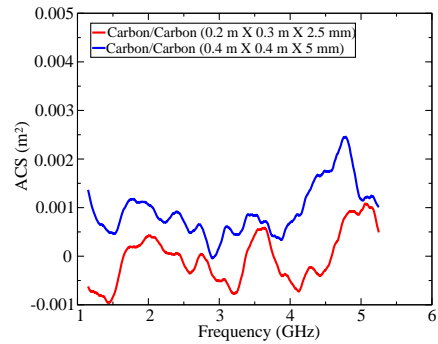penetration depth compared to the sample thickness.
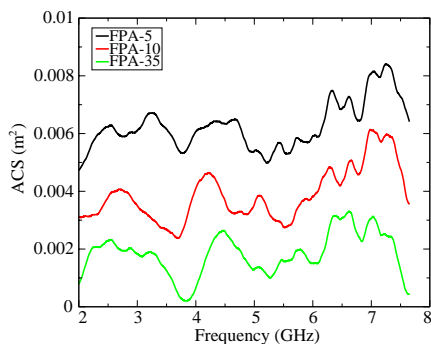
Figure 7. Measured ACS of different carbon foams, having the same dimension.
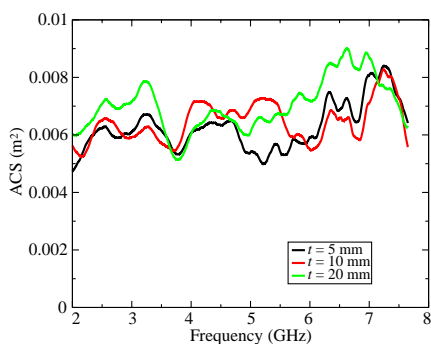
Figure 8. Measured ACS of three slices of FPA-5. Thicknesses are $t = 5\,\text{mm}$, $t = 10\,\text{mm}$, and $t = 20\,\text{mm}$.
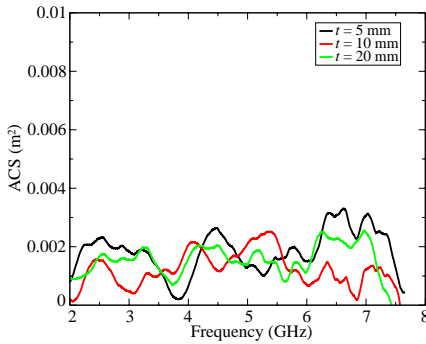
Figure 9. Measured ACS of three slices of FPA-35. Thicknesses are $t = 5\,\mathrm{mm}$, $t = 10\,\mathrm{mm}$, and $t = 20\,\mathrm{mm}$.

Figure 10. Measured ACS of two slices of carbon/carbon.

5.3. Absorbing Cross Section of Carbon/Carbon

We measured the ACS of carbon/carbon samples. The samples were placed on an expanded polystyrene support. Results of measurement are shown in Figure 10. The carbon/carbon have a conductivity much higher than the materials previously tested. As a consequence, we expect high reflections that reduce the ACS. In fact, we observed a very low ACS, whose values are close to the sensitivity of the measurements setup. Therefore carbon/carbon can successfully substitute metals in shielding structures for extreme environment of aerospace applications.

6. CONCLUSION

The RC was successfully used to measure the ACS of absorbing materials, directly related to the absorbed power. The advantage of the RC employment is the capability to generate a random field in terms of polarization, incoming direction and isotropy. Therefore, this kind of excitation is more adherent to the real world operating conditions and yields an averaged ACS. The method is able to detect very small piece of lossy material. The chamber field was also simulated applying a summation of random plane waves, and its coupling to the lossy material was studied by means of a FDTD code able to compute the absorbed power, also for complex geometries. Numerical and experimental data were compared, showing a satisfactory agreement, also for the worst case (smallest sample). Therefore, the simulation technique can be applied to study the absorbing properties of absorbers with arbitrary geometry during the early design stage.

ACKNOWLEDGMENT

REFERENCES

1. Baker-Jarvis, J., "Transmission/reflection and short-circuit line permittivity measurements," Tech. Rep. 1341, NIST, Boulder, CO, USA, 1990.

2. Nicolson, A. M. and G. Ross, "Measurement of the intrinsic properties of materials by time-domain techniques," *IEEE Transactions on Instrumentation and Measurement*, Vol. 19, No. 4, 377–382, 1970.

3. Hasar, U. C., "Microwave method for thickness-independent permittivity extraction of low-loss dielectric materials from transmission measurements," *Progress In Electromagnetics Research*, Vol. 110, 453–467, 2010.

4. Lönnqvist, A., A. Tamminen, J. Mallat, and A. V. Räisänen, "Monostatic reflectivity measurement of radar absorbing materials at 310 GHz," *IEEE Transactions on Microwave Theory and Techniques*, Vol. 54, No. 9, 3486–3491, 2006.

5. Collard, G. and Y. Arien, "Recent microwave absorber wall-reflectivity measurement methods," *IEEE Antennas and Propagation Magazine*, Vol. 50, No. 2, 140–147, 2008.

6. Escot-Bocanegra, D., D. Poyatos-Martnez, I. Montiel-Sanchez, F. M. Saez de Adana, and I. Gonzalez-Diego, "Spherical indoor facility applied to bistatic radar cross section measurements," *Progress In Electromagnetics Research Letters*, Vol. 26, 181–187, 2011.

7. Micheli, D., R. Pastore, C. Apollo, M. Marchetti, G. Gradoni, V. Mariani Primiani, and F. Moglie, "Broadband electromagnetic absorbers using carbon nanostructure-based composites," *IEEE Transactions on Microwave Theory and Techniques*, Vol. 59, No. 10, 2633–2646, 2011.

8. Micheli, D., C. Apollo, R. Pastore, and M. Marchetti, "X-band microwave characterization of carbon-based nanocomposite material, absorption capability comparison and RAS design simulation," *Composites Science and Technology*, Vol. 70, No. 2, 400–409, 2010.

9. Hill, D. A., "Plane wave integral representation for fields in

reverberation chambers," *IEEE Transactions on Electromagnetic Compatibility*, Vol. 40, No. 3, 209–217, 1998.

10. Sorrentino, A., L. Mascolo, G. Ferrara, and M. Migliaccio, "The fractal nature of the electromagnetic field within a reverberating chamber," *Progress In Electromagnetics Research C*, Vol. 27, 157–167, 2012.

11. Moglie, F. and V. Mariani Primiani, "Analysis of the independent positions of reverberation chamber stirrers as a function of their operating conditions," *IEEE Transactions on Electromagnetic Compatibility*, Vol. 53, No. 2, 288–295, 2011.

12. Moglie, F. and V. Mariani Primiani, "Numerical analysis of a new location for the working volume inside a reverberation chamber," *IEEE Transactions on Electromagnetic Compatibility*, Vol. 54, No. 2, 238–245, 2012.

13. Hong, J.-I. and C.-S. Huh, "Optimization of stirrer with various parameters in reverberation chamber," *Progress In Electromagnetics Research*, Vol. 104, 15–30, 2010.

14. Remley, K. A., S. J. Floris, H. A. Shah, and C. L. Holloway, "Static and dynamic propagation-channel impairments in reverberation chambers," *IEEE Transactions on Electromagnetic Compatibility*, Vol. 53, No. 3, 589–599, 2011.

15. Centeno, A. and N. Alford, "Measurement of zigbee wireless communications in mode-stirred and mode-tuned reverberation chamber," *Progress In Electromagnetics Research M*, Vol. 18, 171–178, 2011.

16. Staniec, K. and A. J. Pomianek, "On simulating the radio signal propagation in the reverberation chamber with the ray launching method," *Progress In Electromagnetics Research B*, Vol. 27, 83–99, 2011.

17. Pomianek, A. J., K. Staniec, and Z. Joskiewicz, "Practical remarks on measurement and simulation methods to emulate the wireless channel in the reverberation chamber," *Progress In Electromagnetics Research*, Vol. 105, 49–69, 2010.

18. Mariani Primiani, V. and F. Moglie, "Numerical simulation of LOS and NLOS conditions for an antenna inside a reverberation chamber," *Journal of Electromagnetic Waves and Applications*, Vol. 24, Nos. 17–18, 2319–2331, 2010.

19. Lalléchère, S., S. Girard, D. Roux, P. Bonnet, F. Paladian, and A. Vian, "Mode stirred reverberation chamber (MSRC): A large and efficient tool to lead high frequency bioelectromagnetic in vitro experimentation," *Progress In Electromagnetics Research B*, Vol. 26, 257–290, 2010.

20. Moglie, F., V. Mariani Primiani, and A. P. Pastore, "Modeling of the human exposure inside a random plane wave field," *Progress In Electromagnetics Research B*, Vol. 29, 251–267, 2011.

21. Holloway, C. L., D. A. Hill, J. Ladbury, G. Koepke, and R. Garzia, "Shielding effectiveness measurements of materials using nested reverberation chambers," *IEEE Transactions on Electromagnetic Compatibility*, Vol. 45, No. 2, 350–356, 2003.

22. Mariani Primiani, V., F. Moglie, and A. P. Pastore, "Field penetration through a wire mesh screen excited by a reverberation chamber field: FDTD analysis and experiments," *IEEE Transactions on Electromagnetic Compatibility*, Vol. 51, No. 4, 883–891, 2009.

23. Månsson, D. and A. Ellgardt, "Comparing analytical and numerical calculations of shielding effectiveness of planar metallic meshes with measurements in cascaded reverberation chambers," *Progress In Electromagnetics Research C*, Vol. 31, 123–135, 2012.

24. Moglie, F. and A. P. Pastore, "FDTD analysis of plane waves superposition to simulate susceptibility tests in reverberation chambers," *IEEE Transactions on Electromagnetic Compatibility*, Vol. 48, No. 1, 195–202, 2006.

25. Mariani Primiani, V. and F. Moglie, "Numerical simulation of reverberation chamber parameters affecting the received power statistics," *IEEE Transactions on Electromagnetic Compatibility*, Vol. 54, No. 3, 522–532, 2012.

26. Fedeli, D., G. Gradoni, V. Mariani Primiani, and F. Moglie, "Accurate analysis of reverberation field penetration into an equipment-level enclosure," *IEEE Transactions on Electromagnetic Compatibility*, Vol. 51, No. 2, 170–180, 2009.

27. Gradoni, G., F. Moglie, A. P. Pastore, and V. Mariani Primiani, "Numerical and experimental analysis of the field to enclosure coupling in reverberation chamber and comparison with anechoic chamber," *IEEE Transactions on Electromagnetic Compatibility*, Vol. 48, No. 1, 203–211, 2006.

28. West, J. C., C. F. Bunting, and V. Rajamani, "Accurate and efficient numerical simulation of the random environment within an ideal reverberation chamber," *IEEE Transactions on Electromagnetic Compatibility*, Vol. 54, No. 1, 167–173, 2012.

29. Zhao, H. and Z. Shen, "Memory-efficient modeling of reverberation chambers using hybrid recursive update discrete singular convolution-method of moments," *IEEE Transactions on Antennas and Propagation*, Vol. 60, No. 6, 2781–2789, 2012.

30. Carlberg, U., P.-S. Kildal, A. Wolfgang, O. Sotoudeh, and

C. Orlenius, "Calculated and measured absorption cross sections of lossy objects in reverberation chamber," *IEEE Transactions on Electromagnetic Compatibility*, Vol. 46, No. 2, 146–154, 2004.

31. Amador, E., M. Andries, C. Lemoine, and P. Besnier, "Absorbing material characterization in a reverberation chamber," *EMC Europe 2011 York*, 117–122, 2011.

32. El Baba, I., S. Lalléchère, and P. Bonnet, "Numerical total scattering cross section from reverberating electromagnetic experiments," *Progress In Electromagnetics Research Letters*, Vol. 19, 127–135, 2010.

33. Gifuni, A., "On the measurement of the absorption cross section and material reflectivity in a reverberation chamber," *IEEE Transactions on Electromagnetic Compatibility*, Vol. 51, No. 4, 1047–1050, 2009.

34. Taflove, A. and S. C. Hagness, *Computational Electrodynamics: The Finite-difference Time-domain Method,* Artech House, 2nd Edition, 2000.

35. Cerri, G., R. De Leo, V. Mariani Primiani, and F. Moglie, "Theoretical and experimental analysis of the field-to-line coupling in a reverberation chamber," *IEE Proceedings on Science, Measurement and Technology*, Vol. 153, No. 5, 201–207, 2006.

36. Weisstein, E. W., "Sphere point picking," MathWorld — A Wolfram Web Resource, http://mathworld.wolfram.com/SpherePoint-Picking.html, 2012.

37. International Standards — IEC 61000-4-21, *Electromagnetic compatibility (EMC) — Part 4-21: Testing and Measurement Techniques — Reverberation Chamber Test Methods*, 2.0 Edition, Geneva, Switzerland, 2011.

38. Vaccari, A., A. Cala' Lesina, L. Cristoforetti, and R. Pontalti, "Parallel implementation of a 3D subgridding FDTD algorithm for large simulations," *Progress In Electromagnetics Research*, Vol. 120, 263–292, 2011.

39. Moglie, F., D. Micheli, S. Laurenzi, M. Marchetti, and V. Mariani Primiani, "Electromagnetic shielding performance of carbon foams," *Carbon*, Vol. 50, No. 5, 1972–1980, 2012.